Detection of mantle plumes in the lower mantle by diffraction tomography: theory

Ying Ji, Henri-Claude Nataf[*]

CNRS URA 1316, Départment Terre–Atmosphère–Océan, Ecole Normale Supérieure, 24, rue Lhomond, 75231 Paris Cedex 05, France

Abstract

We investigate the properties of long-period seismic waves scattered by idealized plume conduits in the lower mantle. We build a schematic, yet realistic, model of the seismic velocity and density anomalies caused by a thermal plume. We devise a method to construct realistic seismograms of P-waves scattered by this anomaly. The results show that the scattered wave takes the form of an Airy phase, which arrives after the direct P-wave, at a time that corresponds to the shortest time it takes for the P-wave to travel from the source to the plume, and from there to the station. The predicted amplitude at a long period ($T \simeq 20$ s) is in the range of 1–5% of the amplitude of the direct wave. We explore the variation of the amplitude as a function of the geometrical parameters, and show that it is well explained by considering the contribution of the column of the plume in a $T/4$ Fresnel zone around the fastest scattered ray. We compare the amplitudes and waveforms obtained in the Rayleigh and Mie approximations, and find that, for realistic geometries, wider plumes yield a larger signal. Nevertheless, the predicted amplitudes are too small to yield a detectable signal. In the Born approximation, the image reconstruction of nearly vertical features reduces to a 2D linear inversion. We present a method, based on LSQR, to produce such images from the global set of long-period seismograms. In a companion paper [Ying Ji, H.-C. Nataf, Earth Planet. Sci. Lett., this issue], this method is applied to real data that sample the lower mantle beneath Hawaii. © 1998 Elsevier Science B.V. All rights reserved.

Keywords: diffraction; tomography; heterogeneity; wave dispersion; mantle plumes

1. Introduction

Tomographic models show very weak heterogeneities in the lower mantle except in the D″ layer above the core–mantle boundary [1–4]. The lower mantle also displays a very smooth radial structure down to D″ [5–7]. Nevertheless, from a convection point of view, we expect some heterogeneities in the lower mantle, linked with uprising and downwelling convective currents. Slab-like features have already been detected there [8–10]. The detection of plume conduits remains a tantalizing challenge [11]. Convective models of thermal plumes built to explain hotspot volcanism display conduits with diameters in the range of 100–400 km, and temperatures of 200–400 K, which could translate into 2–5% velocity anomalies. Such narrow and weak heterogeneities are extremely difficult to detect in 'classical' travel-time tomography, although encouraging results have

* Corresponding author.
E-mail: henri-claude.nataf@obs.ujf.grenoble.fr

been obtained [11–14]. Here we explore an alternative approach, which takes advantage of the expected small diameters and large vertical extent of plume conduits. We investigate how plumes could scatter long-period body waves, and how these waves could be used to detect and image mantle plumes.

Our approach can be seen as a special kind of diffraction tomography. Diffraction tomography has become a widely used tool in exploration geophysics (for example [15,16]), and is the subject of important mathematical developments (e.g. [17]). Its application to earthquake seismology is more recent [18] (also see [19] for diffraction tomography of surface waves). In recent years, methods based on isotropic scattering have been proposed to map scatterers in the D'' region at the base of the mantle [20,21] or in the crust [22] and upper mantle [23]. Here, we propose a more complete treatment in the case of nearly vertical line-scatterers.

This paper is organized as follows. In Section 2 we set up a very schematic, yet realistic, model of a thermal mantle plume. In Section 3 we present how to compute synthetic seismograms for waves scattered by a plume. Section 4 gives the properties of these scattered waves. Section 5 describes a method of image reconstruction of plume-like heterogeneities in the lower mantle that makes use of these properties. This method is applied to real data in a companion paper [24].

2. A schematic thermal plume model

In order to compute synthetics of the scattered waves, we establish a very simple thermal plume model. As shown in Fig. 1, we consider a vertical cylinder extending from the core–mantle boundary up to the surface. In a horizontal cross-section, we prescribe a temperature anomaly of a gaussian shape: $\delta T(\xi) = \Delta T_0 \cdot \exp(-\xi^2/a^2)$. It is difficult to know what value should be taken for the maximum temperature anomaly ΔT_0 and for the plume radius a. In the upper mantle, a temperature of about 300 K has been deduced from petrological and dynamical modelling [25,26]. In this study, we target the lower mantle. The temperature anomaly should be larger there, especially if the lower mantle is 30 times more viscous than the upper mantle, as suggested by geoid studies
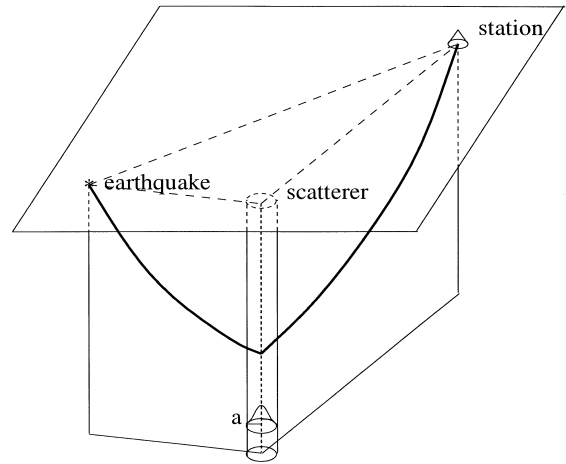

Fig. 1. Schematic set-up. The thermal plume is modelled as a vertical cylinder extending from the surface to the core–mantle boundary. In a horizontal cross-section, a gaussian-shape temperature excess is prescribed, with a radius a (at $1/e$) of 125 km. We consider P-waves that are scattered by the plume off the great circle that joins the earthquake to the station.

[27,28]. Temperature variations across the thermal boundary layer at the base of the mantle could reach 1000 K [29]. In our model, we will assume that ΔT_0 is constant and equals 600 K. The radius of plumes is also very uncertain. It strongly depends upon the variation of viscosity and temperature in the lower mantle. We choose rather arbitrarily $a = 125$ km. We will discuss other choices later in this paper. In order to convert the temperature variation into variations of the elastic parameters and density, we use the following relations inferred by Stacey [30] for a depth of 1400 km:

$$\frac{\partial \ln \alpha}{\partial T} = -3 \times 10^{-5} \, \text{K}^{-1} \tag{1}$$

$$\frac{\partial \ln \beta}{\partial T} = -6.5 \times 10^{-5} \, \text{K}^{-1} \tag{2}$$

$$\frac{\partial \ln \rho}{\partial T} = -1.5 \times 10^{-5} \, \text{K}^{-1} \tag{3}$$

where α and β are the P- and S-wave velocities, and ρ is the density. We keep these values constant throughout the entire mantle. It is expected that they should in fact decrease as one gets deeper into the mantle, but the overall heterogeneity might remain stable since the temperature anomaly in the plume is

expected to increase with depth. Note that the maximum P-velocity anomaly we obtain is only 1.8%, and that the maximum integrated time-anomaly for a P-wave that would travel horizontally across the plume is 0.33 s. We end up with a very simple and schematic thermal plume model, which we think is realistic. In the following, it will be simplified even further, since we will assume that long-period body waves see the plume cylinder as a line. Unless otherwise specified, all computations in this paper are done for this reference idealized thermal plume.

Recent seismic observations suggest velocity contrasts in excess of 10% at the very base of the mantle [31], much larger than what would be produced by thermal variations alone. In the last section, we will discuss how these effects could affect our predictions.

3. Synthetics for scattered P-waves

In order to assess whether waves scattered by a plume could be detected, we need to compute synthetics of these waves in a realistic Earth. The displacement field $u(x)$ at a given position x is expressed as the sum of a 'primary wave' $u_0(x)$ and a 'scattered wave' $u_1(x)$:

$$u(\mathbf{x}) = u_0(\mathbf{x}) + u_1(x) \tag{4}$$

The primary wave consists of various body waves that propagate from the source to the station in the reference Earth model. We will mainly consider the direct P-wave, but one could also choose a PcP or P_{diff} wave, as the primary wave. The scattered wave obeys the wave equation in that same model, but with equivalent source terms that describe the interaction of the primary waves when they hit the scatterer [32]. Therefore, we isolate the propagation steps (from the earthquake to one element of the plume, and from that element to the station), and the interaction step, which describes how to get the equivalent source term at one element from the incoming primary wave.

Let us first consider the interaction step. Since the plume-anomaly we consider is small, we apply the Born approximation, and neglect multiple scattering. Furthermore, we consider the Rayleigh limit which holds when the wavelength is much larger than the

diameter of the plume. Then, the phase difference of the waves scattered by the various parts of a horizontal slice of the plume can be neglected, and one equivalent point source term describes the contribution of one slice. We discuss the applicability of this approximation to waves with a period of 20 s later in this paper. The total scattered field is obtained by summing the contributions from all the slices of the plume, which is seen as a vertical line. The equivalent source terms are easily derived from the displacement $u(x_H)$ of the incoming primary wave at the position x_H of the plume element, and from the plume anomaly, expressed in:

$$\overline{\delta}\rho = (1)/(V) \int \delta\rho \, \mathrm{d}v$$

$$\overline{\delta}\lambda = (1)/(V) \int \delta\lambda \, \mathrm{d}v$$

$$\overline{\delta}\mu = (1)/(V) \int \delta\mu \, \mathrm{d}v$$

where λ and μ are the elastic Lamé parameters [32], and the integration is over the volume V of a slice treated as point. To simplify the notation, we rotate the coordinate system so that the receiver lies at zero azimuth, and we consider only the source and receiver displacement components in the plane of propagation, since we treat only incoming and scattered P-waves. The source term contains an equivalent single force [1], which in the frequency domain is given by:

$$f_\theta = \omega^2 \overline{\delta}\rho V u_\theta \tag{5}$$

$$f_r = \omega^2 \overline{\delta}\rho V u_r \tag{6}$$

and a moment tensor:

$$M_{\theta\theta} = -\mathrm{i}\omega\overline{\delta}\lambda V \left(\frac{p}{r} u_\theta \pm q u_r \right) - 2\mathrm{i}\omega\overline{\delta}\mu V \frac{p}{r} u_\theta \tag{7}$$

$$M_{\theta r} = -\mathrm{i}\omega\overline{\delta}\mu V \left(\frac{p}{r} u_r \pm q u_\theta \right) \tag{8}$$

---

[1] Note that the single force expression is wrong in Aki and Richards [32], as shown in Tarantola [33]. As pointed out by Michael Korn (pers. commun., 1996), the correct expressions are in Wu and Aki [34], and Korn [35], for example.

$$M_{r\theta} = -i\omega\overline{\delta}\mu V \left(\pm q u_\theta + \frac{p}{r} u_r\right) \qquad (9)$$

$$M_{rr} = -i\omega\overline{\delta}\lambda V \left(\frac{p}{r} u_\theta \pm q u_r\right) \mp 2i\omega\overline{\delta}\mu V \cdot q u_r \qquad (10)$$

where u_θ, u_r are the horizontal and vertical components of the far field displacement of the incoming wave, ω is the angular frequency, and r is the radius at the scatterer position. The upper sign refers to a downgoing ray at the scatterer, and the lower sign to an upgoing ray. The ray parameter p, and q, are given by:

$$p = r \frac{\sin i}{\alpha} \qquad (11)$$

$$q = \frac{\cos i}{\alpha} \qquad (12)$$

where i is the incidence angle of the incoming wave. The interaction depends on the characteristics of the incoming wave, but also on the type of anomaly in the plume. Fig. 2 shows the total scattering radiation pattern, and its individual contributions due to $\delta\rho$ (single force term), $\delta\lambda$ (explosion-type moment tensor), and $\delta\mu$ (double-couple moment tensor). We observe that the scattering is largest in the backward direction, where the $\delta\mu$ and $\delta\rho$ terms have the same sign. The $\delta\lambda$ term slightly reduces the effect because it is always negative. This comes from the fact that $(\partial\ln\lambda)/(\partial T)$ seems to be positive in the lower mantle [30].

We now turn to the treatment of the propagation steps. There are many methods to compute synthetic seismograms in a spherical Earth. In this paper we choose to use geometrical ray theory to compute the propagation steps. This theory breaks down when caustics or discontinuities are encountered. This is not a serious limitation, since we are focusing on P-waves that sample the lower mantle, except that we cannot include waves diffracted around the core–mantle boundary. With geometrical ray theory, travel-times t_P are easily computed, and the displacement is given by:

$$u_\theta = A_f(r, r_0) \cdot \sin i \cdot (f_\theta \cdot \sin i_0 \pm f_r \cdot \cos i_0)$$
$$\times e^{-i\omega(t-t_P)} \qquad (13)$$

$$u_r = \pm A_f(r, r_0) \cdot \cos i \cdot (f_\theta \cdot \sin i_0 \pm f_r \cdot \cos i_0)$$
$$\times e^{-i\omega(t-t_P)} \qquad (14)$$

where

$$A_f(r, r_0) = \frac{1}{4\pi\Re(r, r_0)\sqrt{\rho(r_0)\rho(r)\alpha^3(r_0)\alpha(r)}}$$

for a single force, and:

$$u_\theta = A_m(r, r_0) \cdot \sin i \cdot (\dot{M}_{\theta\theta} \cdot \sin^2 i_0$$
$$\pm \dot{M}_{r\theta} \cdot \sin i_0 \cdot \cos i_0 + \dot{M}_{rr} \cos^2 i_0)$$
$$\times e^{-i\omega(t-t_P)} \qquad (15)$$

$$u_r = \pm A_m(r, r_0) \cdot \cos i \cdot (\dot{M}_{\theta\theta} \cdot \sin^2 i_0$$
$$\pm \dot{M}_{r\theta} \cdot \sin i_0 \cdot \cos i_0 + \dot{M}_{rr} \cos^2 i_0)$$
$$\times e^{-i\omega(t-t_P)} \qquad (16)$$

where

$$A_m(r, r_0) = \frac{1}{4\pi\Re(r, r_0)\sqrt{\rho(r_0)\rho(r)\alpha^5(r_0)\alpha(r)}}$$

for the moment tensor, where the subscript $_0$ denotes the source, r is the radius at the receiver, and $\Re(r, r_0)$ is the geometrical spreading [32]. The upper (lower) sign outside the brace refers to a downgoing (upgoing) ray at the receiver. The same applies for the ray at the source within the brace. Note that the time derivative of the moment tensor appears in Eqs. 15 and 16. For this reason, both the force term and the moment tensor term yield a scattered wave that behaves as the second time derivative (ω^2) of the incoming wave. In fact, for an explosive source $M_{ij} = M_0(t)\delta_{ij}$ and introducing the angle Φ between the rays of incoming and scattered waves, the amplitude of the scattered P-wave simply reads:

$$u^{P-P} = \omega^2 \cdot M_0 A_m(r_c, r_0) A_f(r, r_c)\rho(r_c)V$$
$$\times \left[\frac{\overline{\delta}\rho}{\rho(r_c)}\cos\Phi - \frac{\overline{\delta}\lambda}{\lambda(r_c) + 2\mu(r_c)}\right.$$
$$\left. - \frac{2\overline{\delta}\mu}{\lambda(r_c) + 2\mu(r_c)}\cos^2\Phi\right] e^{-i\omega(t-t_1-t_2)} \qquad (17)$$

where t_1 is the travel time from the source to the scatterer, and t_2 from the scatterer to the receiver. r_c is the radius at the scatterer position.

4. Properties of waves scattered by a plume

We first examine one example of a P-wave scattered by a plume-like vertical line. In Fig. 3a, we
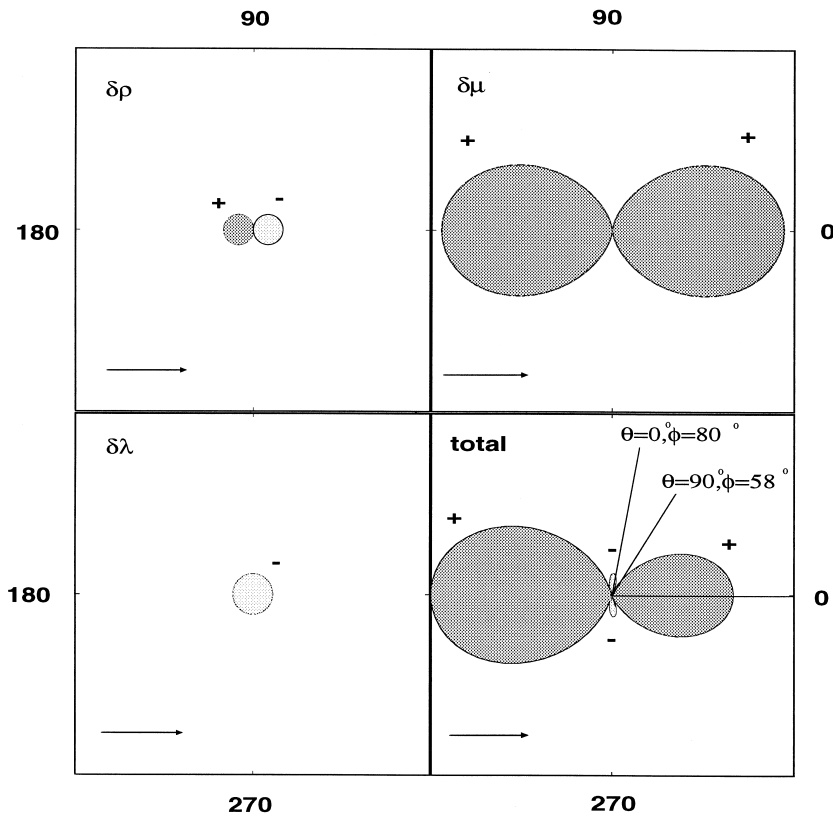
Fig. 2. P→P scattering radiation pattern for a thermal plume-like anomaly in the lower mantle. We plotted the amplitude of the scattered wave in a polar diagram (angles in degrees). The horizontal axis is the direction of the incoming wave, which arrives from the left. The sign of the amplitude is indicated by the shading. All amplitudes are normalized to the maximum amplitude of the total radiation pattern (bottom right). The other panels give the contributions of the $\delta\rho$, $\delta\mu$, and $\delta\lambda$ terms. Also drawn is the wedge in which scattering takes place for the realistic geometries discussed in this paper.

show the waves scattered by the different horizontal slices of the plume. Each 10-km-thick slice is treated as a point (Rayleigh scattering), and carries a perturbation that is the integrated perturbation over the slice. The number on the left gives the depth of the slice, from 1000 km to the core–mantle boundary. The epicentral distance is $\Delta = 70°$. The plume is situated 17° off the great circle that joins the earthquake to the station (see inset of Fig. 4). We see that the travel-time of the wave scattered by the slice at depth 2189 km (thick line) is minimum. We remark that this minimum time is easily determined: it corresponds to the travel-time of a direct P-wave for an epicentral distance $\Delta' = \Delta_1 + \Delta_2$ where Δ_1 is the epicentral distance between the source and the plume, and Δ_2 from the plume to the station. The slices just above and below the 'fastest' slice

produce scattered waves that interfere constructively to form an 'Airy phase'. As a result, the total wave (drawn at the bottom with a factor 1/59) consists in a strong pulse starting at the minimum travel-time. In b, the solid line is the total scattered wave again. One sees a very small wavelet at a time around 900 s: it corresponds to scattering from the top slice of the cylinder. All contributions in between have interfered destructively.

We can pursue this analysis to infer amplitudes. We expect that the slices that contribute to the total scattered wave are those that fall within the Fresnel zone of the fastest scattered wave along the cylinder. Indeed, the dotted line in Fig. 3b shows the seismogram computed with the scattered waves that arrive within a time $T/4$ of the fastest wave (here the dominant period T is 20 s). Another approach is to
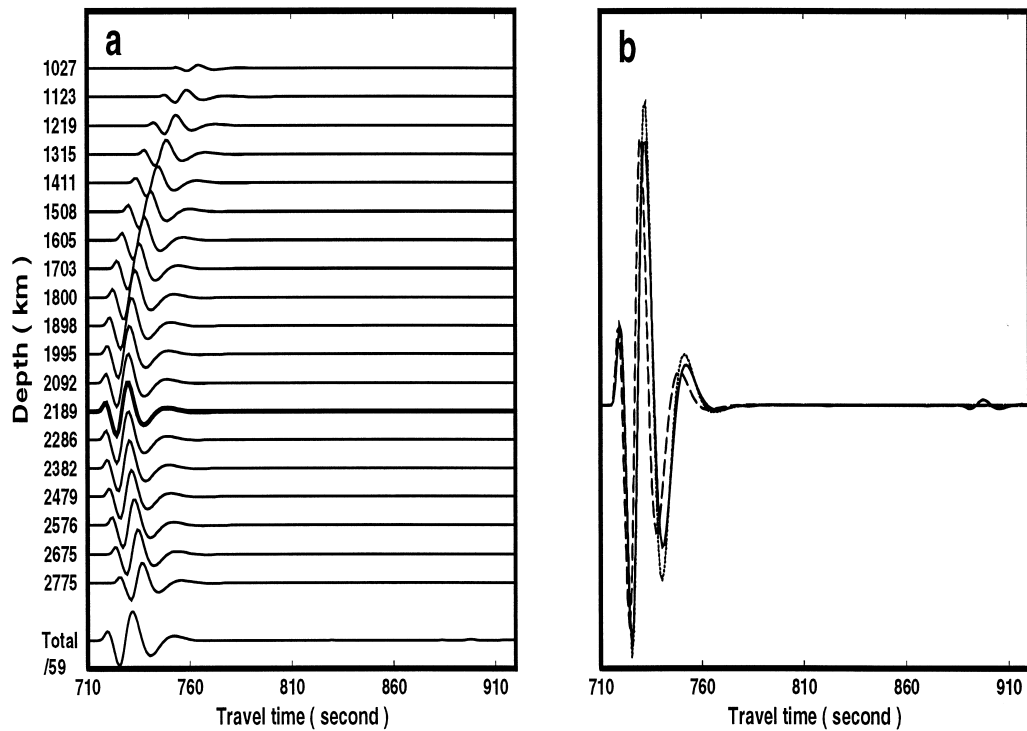
Fig. 3. (a) P → P scattered waves by horizontal slices of the vertical plume at various depths (along the ordinate). The slice at depth 2189 km (thick line) yields the shortest travel-time. At the bottom, the resulting total scattered wave takes the form of an Airy phase starting at the shortest travel-time (the amplitude is scaled down by a factor 59 as compared to the individual contributions from the 10-km-thick slices). (b) Comparison of the total wave (solid line) with the seismogram computed with contributions from only the $T/4$ Fresnel zone (dotted line), and with the seismogram from the slice that yields the shortest travel-time given a height equal to the $T/10$ Fresnel zone (dashed line).

determine what would be the equivalent height we should give to the fastest slice in order that it yields the amplitude of the total wave. This turns out to be the height of the $T/10$ Fresnel zone, as shown by the dashed line. This gives a simple recipe to estimate the amplitude of the scattered wave for various periods. Note that while the amplitude of the wave scattered by a point varies as ω^2, the wave scattered by a line (or a cylinder as long as ω is small enough for Rayleigh scattering to be appropriate) behaves as $\omega^{3/2}$ since the Fresnel zone roughly varies as $\omega^{-1/2}$.

We now examine how the total scattered wave behaves when the plume position is changed. At the bottom of Fig. 4 we show the direct P-wave and the surface-reflecting PP-wave for an epicentral distance $\Delta = 70°$. Both the source and the receiver are at the surface. The source is explosive. The impulse response has been convolved with a typical

long-period SRO instrument response, and attenuation with $t^* = 1$ s. At a scale 75 times larger are drawn the scattered waves we compute for various positions of the plume, as shown in the inset. Note that the amplitude of the scattered wave decreases as the plume gets farther away from the great circle that joins the receiver to the source. At intermediate distances, the amplitude of the scattered wave reaches 2% that of the direct wave, while the maximum P-velocity anomaly is only 1.8%. This is due to the vertical extent of the plume and the formation of the 'Airy phase'. Indeed, in Fig. 4 we have plotted the shortest arrival time; it corresponds very well with the onset of the computed scattered wave.

For a given epicentral distance Δ from source E to station R, we can consider all the hypothetical plume positions H for which $EH + HR = \Delta'$ is constant, and therefore yield the same arrival time
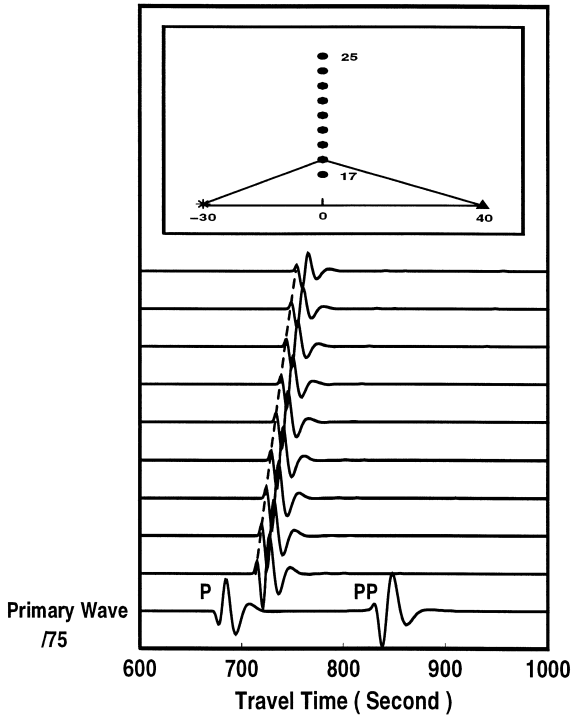
Fig. 4. Synthetic seismograms of waves scattered by a thermal mantle plume. The direct P- and PP-waves are shown at the bottom. The epicentral distance is $\Delta = 70°$. The seismograms include the SRO instrument response, and attenuation. The scattered waves for different positions of the plume are drawn at the same scale (which is 75 times larger than the scale for the direct wave). The inset displays the geometry for the different seismograms.

for the scattered wave. In Cartesian geometry all the points H would lie on an ellipse at the surface. On the sphere, we obtain the surface locus of the hypothetical vertical plumes from:

$$\cos^2 OH = \frac{\sin^2 \frac{\Delta'}{2} - \sin^2 \frac{\Delta}{2} \cdot \cos^2 \theta}{\cos^2 \frac{\Delta}{2} \cdot \tan^2 \frac{\Delta'}{2} - \sin^2 \frac{\Delta}{2} \cdot \cos^2 \theta} \quad (18)$$

where the angle θ is defined in Fig. 5, and O is the mid-point between E and R. In Fig. 6, we examine how the amplitude of the scattered wave varies with θ for various (Δ, Δ') couples. We consider an explosive source and plot the ratio of the scattered wave over the direct wave for the vertical component. For actual earthquakes, the radiation would modulate the
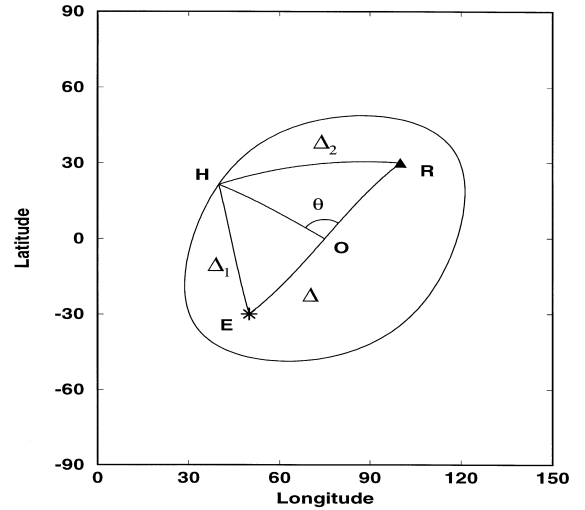

Fig. 5. Geometric relations for scattering by a vertical plume. E and R are the positions of the source and receiver at the surface ($ER = \Delta$). The mid-point a the surface between E and R is noted O. The 'ellipse' corresponds to points such as H, for which the cumulated epicentral distance $EH + HR$ is constant and equals Δ'. We introduce the angle θ between OH and OR.

pattern we compute, but this can easily be accounted for. For reasons of symmetry we only need to consider $0 \le \theta \le \pi/2$. For $\theta > 20°$, the scattered wave is positive: we are in the forward-scattering quadrant of Fig. 2. We observe that the amplitude ratio is fairly constant in this range. This is the result of the competition between two effects: when θ increases, the scattering angle Φ decreases and reaches a minimum at $\theta = \pi/2$; this yields a maximum amplitude, but at the same time the effect of geometric spreading is to reduce the amplitude of the scattered wave as θ increases. Below $\theta \simeq 20°$ we note that the sign of the scattered wave becomes negative. We enter the negative lobe of Fig. 2, for a scattering angle Φ slightly less than $\pi/2$. Note that for $\theta = 0°$, we have pure back-scattering in the horizontal plane, but since the ray changes angle in the vertical plane, the actual scattering angle Φ is in fact not far from 90°. In Fig. 2 we show one example in which the variation of the scattering angle Φ is between 80° and 58° when the θ angle varies from 0° to 90°.

The analysis of the scattered wave in terms of an Airy phase suggests that its amplitude could be predicted by taking into account only the portion of the plume for which the scattered wave is the fastest.
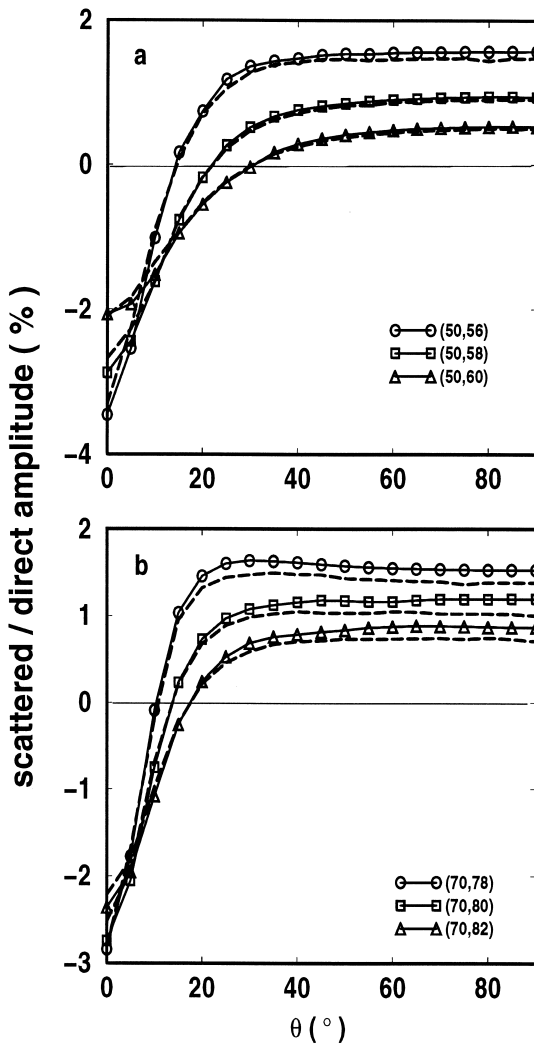
Fig. 6. Amplitude of the scattered wave over the amplitude of the direct wave as a function of the angle θ, for various (Δ, Δ') couples. (a) $\Delta = 50°$; (b) $\Delta = 70°$. The dashed lines represent the contribution of the fastest slice, given a height equal to the $T/10$ Fresnel Zone.

The dashed lines in Fig. 6 are these predictions when the height given to the slice of the plume that yields the minimal travel-time is equal to the $T/10$ Fresnel zone. We find that the prediction is very good.

In Fig. 6, we observe that the amplitude ratio is rather constant around $\theta = \pi/2$, and is a strong function of Δ'. In Fig. 7, we plot the amplitude ratio at $\theta = \pi/2$ as a function of the time separation between the direct and the scattered wave for various
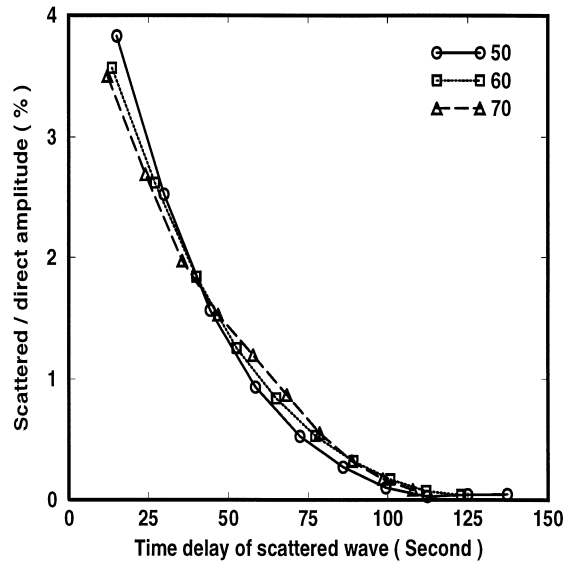

Fig. 7. Amplitude of the scattered wave over the amplitude of the direct wave as a function of the time separation between these two waves, for various values of Δ, at $\theta = \pi/2$. The points are computed for Δ' increments of 2°, starting at $\Delta + 2°$.

values of Δ. We observe that all ratios almost fall along the same curve. The smaller the time separation, the larger the amplitude of the scattered wave. In practice, one will look for scattered waves that arrive late enough behind the direct wave to be well separated. For long-period seismograms with a dominant period of 20 s, a time-separation of 40 s should be safe enough. This yields typical amplitude ratios of 1.5%.

In Fig. 8, we plot the depth of intersection of the fastest scattered wave with the plume and the $T/10$ Fresnel zone as a function of θ, for various (Δ, Δ') couples. For all cases considered, the plume is probed in the lower mantle.

So far, we have treated the plume cylinder as a line. Each slice of the cylinder is viewed as a point. This is the Rayleigh approximation, which is valid when the wavelength of the incoming wave is small as compared to the typical dimension of the scatterer. For P-waves of period $T = 20$ s, the wavelength is about 260 km. This guided our choice of 125 km for the plume radius. Clearly, for larger values (geodynamically plausible), the Rayleigh approximation will break down, and we should turn to the Mie approximation, in which waves scattered by
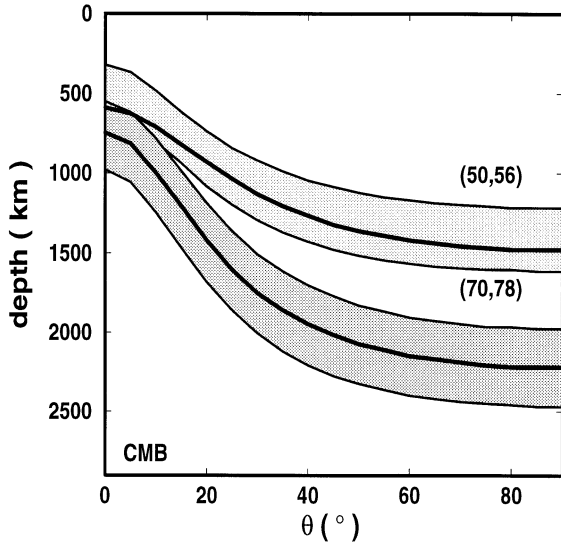
Fig. 8. Intercept depth of the fastest scattered wave with the vertical plume as a function of θ. Also drawn are the limits of the $T/10$ Fresnel zone on both sides.

Fig. 9. Comparison of the amplitudes of the P → P scattered waves in the Rayleigh (squares) and Mie (circles) approximations as a function of plume radius, for the scattering geometry depicted in the inset. The solid symbols mark the results for our reference radius of 125 km.

different points in a slice can interfere (note that our 'Rayleigh' scattering treatment already takes into account interferences of waves scattered by slices at different depths). In the Mie approximation, we split each horizontal slice into ten angular sectors and twenty radial rings and sum the resulting individual scattered waves. In Fig. 9, we compare the amplitudes obtained in the Mie and Rayleigh approximations for a typical scattering geometry, depicted in the inset, as a function of the plume radius. The amplitudes are overestimated in the Rayleigh approximation (upper curve). For our case with a radius of 125 km, the difference is about 25%. It is interesting to note that the correct (Mie scattering) amplitudes continue to increase when the radius of the plume increases. Thus the actual amplitude of the wave scattered by a 200-km-radius plume could be about 50% times larger than our estimates (based on the Rayleigh approximation) for a 125-km-radius plume. Note that the difference between the Rayleigh and Mie amplitudes strongly depends on the scattering angle [34]. In particular, back-scattering is much more affected by the interferences than forward-scattering. We have seen that in realistic geometries, scattering mainly takes place in the forward quadrant in our case. This explains why the Rayleigh approx-
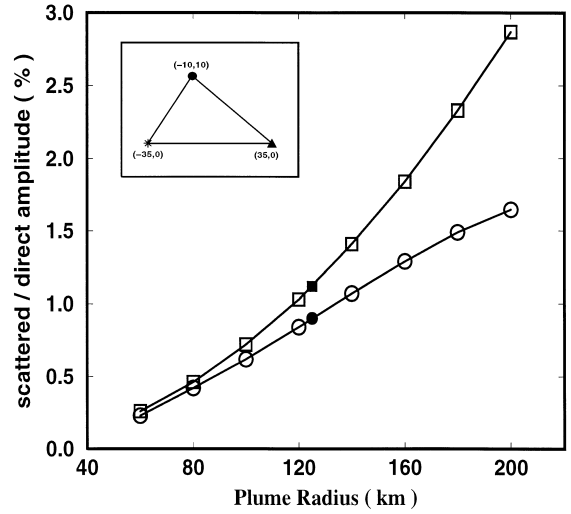
imation remains appropriate for rather large plume radii.

5. Image reconstruction

In the Born approximation, the general expression in the frequency domain for the amplitude of P → P scattered waves by heterogeneities distributed in volume follows from Eq. 17:

$$
\begin{aligned}
u^{\text{P–P}} = \omega^2 \dot{M}_0 \int_V & A_{\text{m}} A_{\text{f}} \rho(r_{\text{c}}) \\
\times & \left[\frac{\delta\rho}{\rho(r_{\text{c}})} \cos\Phi - \frac{\delta\lambda}{\lambda(r_{\text{c}}) + 2\mu(r_{\text{c}})} \right. \\
& \left. - \frac{2\delta\mu}{\lambda(r_{\text{c}}) + 2\mu(r_{\text{c}})} \cos^2\Phi \right] e^{-i\omega(t-t_1-t_2)} \, dV
\end{aligned}
$$
(19)

where the integration is over the whole volume of interest. As usual for the Born approximation, this amplitude is related linearly to the perturbations we want to retrieve. We have assumed an explosive source. For actual earthquakes, the amplitude will be modulated by the radiation pattern. This is easily accounted for in the inversion scheme. Here, we lump the variations in ρ, λ and μ into a single

δT term, assuming Eqs. 1–3. Expressing the logarithmic derivative of a parameter x with respect to temperature as C_x, we get:

$$
\begin{aligned}
u^{\mathrm{P-P}} = \;& \omega^2 \dot{M}_0 \\
& \times \int_V \rho A_{\mathrm{m}} A_{\mathrm{f}} \left(C_\rho \cos \Phi - \frac{C_\lambda + 2 C_\mu \cos^2 \Phi}{\lambda + 2\mu} \right) \\
& \times \delta T \mathrm{e}^{-\mathrm{i}\omega(t - t_1 - t_2)} \, \mathrm{d}V
\end{aligned}
\tag{20}
$$

If we consider that δT is constant along a vertical line, as in our forward analysis, and define $\delta T(\theta, \phi)$, the expression becomes:

$$
\begin{aligned}
u^{\mathrm{P-P}} = \;& \omega^2 \dot{M}_0 \iint_S \left[\int_0^{CMB} \rho A_{\mathrm{m}} A_{\mathrm{f}} \right. \\
& \times \left(C_\rho \cos \Phi - \frac{C_\lambda + 2 C_\mu \cos^2 \Phi}{\lambda + 2\mu} \right) \\
& \left. \times \mathrm{e}^{-\mathrm{i}\omega(t - t_1 - t_2)} \, \mathrm{d}z \right] \delta T(\theta, \phi) \, \mathrm{d}S
\end{aligned}
\tag{21}
$$

The z integral of course depends on θ and ϕ. In practice, an additional simplification can be made to save computer time. Our forward analysis shows that the waveform and amplitude of the wave scattered by a vertical heterogeneity is well predicted by considering the scattered wave computed for the element that yields the fastest ray, multiplied by the volume of the $T/10$ Fresnel zone (see Fig. 3). The integration over depth is then unnecessary.

We are now faced to a 2D imaging problem where the data (the scattered wave amplitude in the frequency domain) is linearly related to the parameter we invert for $[\delta T(\theta, \phi)]$. This is similar to what is obtained for surface waves [19].

The next step is to transform it to a discrete inversion problem by defining a grid at the surface of the Earth. We get:

$$
U = G\Gamma
\tag{22}
$$

where U is the vector of the scattered wave amplitude measured in the seismograms, G is the data kernel easily derived from Eq. 21, and Γ is the unknown model (the temperature perturbation at each grid point).

The system of Eq. 22 is usually inconsistent and underdetermined. It has to be solved by the least square method. We use a damped least square scheme in which we solve the normal equation

$$
(G^{\mathrm{T}} G + \Lambda^2 I)\Gamma = G^{\mathrm{T}} U
\tag{23}
$$

where Λ is a damping constant introduced to stabilize the solution. As usual in tomographic problems, the G matrix is large and extremely sparse. For a typical time-window of 40 s, the area of the ellipse that corresponds to the back-projection of the seismogram covers only 4% of the surface of the Earth. This means that in the global tomographic problem, only 4% of the elements in a row of G are non-zero. Iterative methods are therefore used. Classical methods include the algebraic reconstruction technique (ART) [36], the simultaneous iterative reconstruction technique (SIRT) [36], and the LSQR [37], which is a variant of the conjugate gradient (CG) method. Among these methods, LSQR is known to be better for tomographic problems [38,39]. We therefore use this method here.

In practice, additional simplifications can be made to save computer time. We find that it is sufficient to retain only one frequency component (phase and amplitude) in the data vector U. Note that the pre-processing applied to the data (such as tapering and filtering) should also be applied to the synthetics resulting from G. Our forward analysis indicates that the scattered $P \rightarrow P$ amplitude decreases strongly with the time-delay after the direct P. On the other hand, one has to be far enough from the direct P to avoid source contamination. A good compromise is to consider a time window (50 s, 100 s) after P. Similarly, we found that the amplitude (and sampling depth) of the scattered wave does not depend on the position on the ellipse, except for small θ angles. One can just remove the end points of the ellipse ($\theta < 20°$) from the data.

The performance of the method we propose is illustrated in a companion paper [24].

6. Discussion and conclusion

We have explored a new approach to the detection and imaging of nearly vertical heterogeneities in the mantle, such as plumes. This approach rests on the use of long-period scattered waves, and is akin to diffraction tomography. The vertical extent of the

heterogeneity yields a number of interesting properties. The scattered wave takes the form of an Airy phase. It results from a constructive interference of scattered waves by elements of the vertical line that lie around the element for which the travel-time is minimum. As a consequence, the amplitude of the total scattered wave scales as $\omega^{3/2}$, instead of ω^2 for diffraction by a point, where ω is the frequency. We find that the amplitude of the scattered wave is mostly a function of its time delay after the direct P-wave. The locus of vertical lines that can contribute to a scattered wave arriving at a given time is an ellipse on the sphere. We find that, for realistic geometries, the amplitude is nearly independent of the position on the ellipse, except for lines close to the two focal points of the ellipse: the earthquake epicentre and the station. We use these properties to devise an imaging algorithm. In the Born approximation, the scattered wave is related linearly to the heterogeneity. In the case of vertical heterogeneities, the image reduces to 2D. We propose an algorithm based on LSQR to construct 2D images of vertical anomalies in the lower mantle from the global set of long-period seismograms.

However, one of the conclusions of our analysis is that the predicted signal for realistic thermal plume-like features is very small. The amplitude of the scattered wave only reaches 1–3% that of the direct wave. Such a small signal would be very difficult to extract from the data.

Recent seismic observations suggest very low P velocities in a thin layer (10–40 km) in several geographic locations at the very base of the mantle [31]. The velocity anomalies vary 10% for P-waves and as much as 30% for S-waves. Such anomalies seem too large to be explained by thermal effects alone and partial melting has been invoked [40]. One can imagine that this very slow material could also be present in the core of upwelling plumes. The expected anomaly would then be increased by a factor of 5 as compared to our standard thermal plume model, yielding scattered waves with an amplitude of 5–15% that of the direct wave.

We applied the method to a set of actual seismograms that sample the lower mantle beneath Hawaii. The results, described in a companion paper [24], indicate that a large anomaly is present northwest of Hawaii. The size of the anomaly is about 30– 50 times larger than that predicted by our simple thermal plume model.

Our study is one of the first attempts to apply a kind of diffraction tomography to the mantle. We tried to cover both the forward modelling (with particular attention to the amplitudes), the inversion, and the application to real data (in a companion paper). The results we obtained are encouraging, and possibly exciting. Clearly, further work will be needed to assess the actual potential of this approach for the mapping of heterogeneities in the mantle.

Acknowledgements

References

[1] A.M. Dziewonski, Mapping the lower mantle: determination of lateral heterogeneity in P velocity up to degree and order 6, J. Geophys. Res. 89 (1984) 5925–5929.

[2] H. Inoue, Y. Fukao, K. Tanabe, Y. Ogata, Whole mantle P-wave travel time tomography, Phys. Earth Planet. Inter. 59 (1990) 294–328.

[3] W. Su, R.L. Woodward, A. Dziewonski, Degree 12 model of shear velocity heterogeneity in the mantle, J. Geophys. Res. 99 (1994) 6954–6980.

[4] M. Sylvander, A. Souriau, Mapping S-velocity heterogeneities in the D″ region, from SmKS travel times, Phys. Earth Planet. Inter. 94 (1996) 1–21.

[5] H. Jeffreys, K.E. Bullen, Seismological Tables, British Association for the Advancement of Science, London, 1940.

[6] A.M. Dziewonski, D.L. Anderson, Preliminary reference Earth model, Phys. Earth Planet. Inter. 25 (1981) 297–356.

[7] B.L.N. Kennett, E.R. Engdahl, Traveltime for global earthquake location and phase identification, Geophys. J. Int. 105 (1991) 429–465.

[8] K.C. Creager, T.H. Jordan, Slab penetration into the lower mantle, J. Geophys. Res. 89 (1984) 3031–3049.

[9] R. Van der Hilst, R. Engdahl, W. Spakman, G. Nolet, Tomographic imaging of subducted lithosphere below northwest Pacific island arcs, Nature 353 (1991) 37–43.

[10] S.P. Grand, Mantle shear structure beneath the Americas and surrounding oceans, J. Geophys. Res. 99 (1994) 11591–11621.

[11] H.-C. Nataf, J. VanDecar, Seismological detection of a mantle plume?, Nature 364 (1993) 115–120.

[12] M. Granet, G. Stoll, J. Dorel, U. Achauer, G. Poupinet, K. Fuchs, Massif Central (France): new constraints on the geodynamical evolution from teleseismic tomography, Geophys. J. Int. 121 (1995) 33–48.

[13] J.C. VanDecar, D.E. James, M. Assumpcao, Seismic evidence for a fossil mantle plume beneath South America and implications for plate driving forces, Nature 378 (1995) 25–31.

[14] C.J. Wolfe, I.Th. Bjarnason, J.C. VanDecar, C. Solomon, Seismic structure of the Iceland mantle plume, Nature 385 (1997) 245–247.

[15] A.J. Devaney, Geophysical diffraction tomography, IEEE Trans. Geosci. Remote Sensing 22 (1984) 3–13.

[16] R.S. Wu, M.N. Toksöz, Diffraction tomography and multisource holography applied to seismic imaging, Geophysics 52 (1987) 11–25.

[17] V.M. Buchstaber, V.K. Maslov, Mathematical models and algorithms of tomographic synthesis of wavefields and inhomogeneous media, in: Gelfand I.M., Gindikin, S.G. (Eds.), Problems of Tomography, American Mathematical Society, 81 (1990) 267 pp.

[18] D.J. Doornbos, Diffraction seismic tomography, Geophys. J. Int. 108 (1992) 256–266.

[19] R. Snieder, 3-D linearized scattering of surface waves and a formalism for surface wave holography, Geophys. J. R. Astron. Soc. 84 (1986) 581–605.

[20] T. Lay, C.J. Young, Imaging scattering structures in the lower mantle by migration of long-period S waves, J. Geophys. Res. 101 (1996) 20023–20040.

[21] F. Scherbaum, F. Krüger, M. Weber, Double beam imaging: mapping lower mantle heterogeneities using combinations of source and receiver arrays, J. Geophys. Res. 102 (1997) 507–522.

[22] J. Revenaugh, The contribution of topographic scattering to teleseismic coda in southern California, Geophys. Res. Lett. 22 (1995) 543–546.

[23] J. Revenaugh, A scattered-wave image of subduction beneath the transverse ranges, Science 268 (1995) 1888–1892.

[24] Ying Ji, H.-C. Nataf, Detection of mantle plumes in the lower mantle by diffraction tomography: Hawaii. Earth Planet. Sci. Lett. 159 (1998) (this issue).

[25] S. Watson, D. McKenzie, Melt generation by plumes: a study of Hawaiian volcanism, J. Petrol. 32 (1991) 501–537.

[26] N.M. Ribe, U.R. Christensen, Melt generation by plumes: a study of Hawaiian volcanism, J. Geophys. Res. 99 (1994) 669–682.

[27] B.H. Hager, Subducted slabs and the geoid: constraints on mantle rheology and flow, J. Geophys. Res. 89 (1984) 6003–6016.

[28] Y. Ricard, C. Vigny, C. Froidevaux, Mantle heterogeneities, geoid, and plate motion: a Monte Carlo inversion, J. Geophys. Res. 94 (1989) 13739–13754.

[29] R. Boehler, Melting of the Fe–FeO and Fe–FeS systems at high pressure: constraints on core temperatures, Earth Planet. Sci. Lett. 111 (1992) 217–227.

[30] F.D. Stacey, Theory of thermal and elastic properties of the lower mantle and core, Phys. Earth Planet. Inter. 89 (1995) 219–245.

[31] E.J. Garnero, D.V. Helmberger, A very slow basal layer underlying large-scale low-velocity anomalies in the lower mantle beneath the Pacific: evidence from core phases, Phys. Earth Planet. Inter. 91 (1995) 161–176.

[32] K. Aki, P.G. Richards, Quantitative Seismology, Theory and Methods, Freeman, San Francisco, CA, 1980.

[33] A. Tarantola, Inversion of travel times and seismic waveforms, in: G. Nolet (Ed.), Seismic Tomography, Reidel, Dordrecht, 1987.

[34] R.S. Wu, K. Aki, Scattering characteristics of elastic waves by an elastic heterogeneity, Geophysics 50 (1985) 582–595.

[35] M. Korn, Seismic waves in random media, J. Appl. Geophys. 29 (1993) 247–269.

[36] G.T. Herman, Image Reconstruction from Projections, the Fundamentals of Computerized Tomography, Academic Press, London, 1980.

[37] C.C. Paige, M.A. Saunders, LSQR: an algorithm for sparse linear equations and sparse least squares, ACM Trans. Math. Software 8 (1982) 43–71.

[38] A. van der Sluis, H.A. van der Vorst, Numerical solution of large, sparse linear algebraic systems arising from tomographic problems, in: G. Nolet (Ed.), Seismic Tomography, Reidel, Dordrecht, 1987.

[39] G. Nolet, Seismic wave propagation and seismic tomography, in: G. Nolet (Ed.), Seismic Tomography, Reidel, Dordrecht, 1987.

[40] Q. Williams, E.J. Garnero, Seismic evidence for partial melt at the base of earth's mantle, Science 273 (1996) 1528–1530.